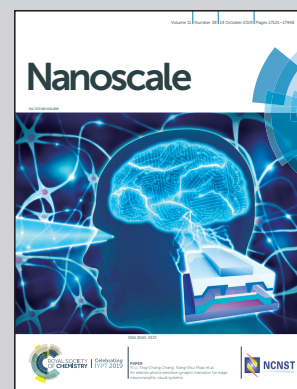**Showcasing research from the Yale Faboratory, School of Engineering and Applied Science, Yale University, United States.**
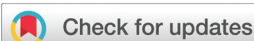
Oxide rupture-induced conductivity in liquid metal nanoparticles by laser and thermal sintering

Gallium-based liquid metals have shown great potential in soft and stretchable electronics. When first printed, films of liquid metal nanoparticles are non-conductive. We present two thermally involved sintering methods – laser and thermal sintering – to achieve electrical conductivity. Our work reveals the oxide rupture-induced mechanisms and shows that thermal and laser sintering under different conditions generate highly conductive liquid, solid or solid-liquid films with tunable morphologies and properties that can be used in soft robotics, wearable electronics, or broad semiconductor applications.

ROYAL SOCIETY OF CHEMISTRY | Celebrating IYPT 2019

rsc.li/nanoscale

Check for updates

Oxide rupture-induced conductivity in liquid metal nanoparticles by laser and thermal sintering†

Shanliangzi Liu, [ID] [a,b] Serrae N. Reed,[b] Matthew J. Higgins,[c] Michael S. Titus[c] and Rebecca Kramer-Bottiglio*[b]

Metallic inks with superior conductivity and printability are necessary for high-throughput manufacturing of printed electronics. In particular, gallium-based liquid metal inks have shown great potential in creating soft, flexible and stretchable electronics. Despite their metallic composition, as-printed liquid metal nanoparticle films are non-conductive due to the surrounding metal oxide shells which are primarily Ga_2O_3, a wide-bandgap semiconductor. Hence, these films require a sintering process to recover their conductivity. For conventional solid metallic nanoparticles, thermal and laser processing are two commonly used sintering methods, and the sintering mechanism is well understood. Nevertheless, laser sintering of liquid metal nanoparticles was only recently demonstrated, and to date, the effect of thermal sintering has rarely been investigated. Here, eutectic gallium–indium nanoparticle films are processed separately by laser or thermal sintering in an ambient environment. Laser and thermally sintered films are compared with respect to electrical conductivity, surface morphology and elemental composition, crystallinity and surface composition. Both methods impart thermal energy to the films and generate thermal stress in the particles, resulting in rupture of the gallium oxide shells and achieving electrical conductivity across the film. For laser sintering, extensive oxide rupture allows liquid metal cores to flow out and coalesce into conductive pathways. For thermal sintering, due to less thermal stress and more oxidation, the oxide shells only rupture locally and extensive phase segregation occurs, leading to non-liquid particle films at room temperature. Electrical conductivity is instead attributed to segregated metal layers and gallium oxide which becomes crystalline and conductive at high temperatures. This comprehensive comparison confirms the necessity of oxidation suppression and significant thermal stress *via* instantaneous laser irradiation to achieve conductive patterns in liquid form.

1. Introduction

Recent advances in the field of soft robotics and wearables have increased the demand for printed soft and flexible electronics.[1–5] Additive manufacturing techniques, such as inkjet printing,[6–9] spray printing[10–12] and aerosol jet printing[9,13–15] are all promising alternatives to conventional lithography-based methods.[3] These techniques may be applicable to roll-to-roll production, paving the way for future mass manufacturing.[16–18] Applying these printing techniques to produce soft and flexible electronics requires functional inks with satisfactory conductivity and printabiliy.[19–22] The main choices of conductive materials include metal nanoparticles,[23,24] carbon-based materials[25] such as carbon nanotubes[26,27] and graphene,[28,29] and conductive polymers.[30,31] With superior electrical conductivity, metal nanoparticles are optimal for utilization in conductive inks. Recent applications of metallic nanoparticles in printed flexible electronics include sensors,[32,33] transistors[34,35] and light-emitting devices,[36,37] *etc*.

Two types of metallic nanoparticles are often used for soft and flexible electronics: conventional solid metal nanoparticles and gallium-based liquid metal nanoparticles. With high conductivity (6.3×10^7 S m^{-1}) and oxidation stability, silver has emerged as the most widely used material in flexible electronics.[33,35,38] However, due to its high cost, copper[39,40] (5.96×10^7 S m^{-1}), aluminum[41,42] (3.78×10^7 S m^{-1}) and nickel[43,44] (1.43×10^7 S m^{-1}) nanoparticles have been utilized as a replacement. The main challenge in implementation of these alternatives is in overcoming the issue of oxidation in ambient conditions, which leads to low electrical conductivity;

School of Mechanical Engineering, Purdue University, West Lafayette, Indiana 47907, USA

School of Engineering and Applied Science, Yale University, New Haven, Connecticut 06511, USA. E-mail: rebecca.kramer@yale.edu

School of Materials Engineering, Purdue University, West Lafayette, Indiana 47907, USA

†Electronic supplementary information (ESI) available. See DOI: 10.1039/c9nr03903a

otherwise, an inert environment would be necessary for manufacturing. Therefore, a layer of metal or other capping agent (thiol, polymer) is often coated on the surface of the nanoparticles to minimize the penetration of oxygen.[45,46] Additionally, a proper dispersing agent is imperative to prevent particle aggregation and sedimentation.[47]

In recent years, gallium-based liquid metals have received tremendous attention in the field of soft and flexible electronics. In particular, eutectic gallium–indium alloy (eGaIn; 75.5 wt% Ga, 24.5 wt% In) has a combination of high electrical conductivity (3.4×10^6 S m^{-1}), low melting temperature (15.5 °C), low viscosity (2 mPa s),[48] negligible vapor pressure[49] and intrinsic softness. One of the most unique properties of gallium-based liquid metals is that the surfaces rapidly react with oxygen to form a thin passivating oxide skin (~1–3 nm in ambient environment;[50–52] ~0.7 nm under vacuum conditions[53,54]) primarily composed of Ga_2O_3. The oxide growth has also been found to be accelerated under elevated temperature.[55] Previously, Hohman et al. demonstrated the ability to create stable liquid metal nanoparticle suspensions in ethanol via ultrasonication.[56] During the sonication process, gallium oxide continuously forms, fractures, and reforms, resulting in smaller nanoparticles. Dispersing agents or other chemical additives are not necessary as the oxide prevents the particles from coalescing. Deposition of liquid metal nanoparticle dispersions using inkjet printing[57] and spray printing techniques[11] has been presented in our previous work.

Both liquid metal and conventional solid metal nanoparticles require an additional sintering step to recover metallic conductivity after deposition. For conventional metallic nanoparticles, the presence of insulating stabilizing agents or chemical additives around the particles prevents direct contacts between particles and results in low electrical conductivity. Therefore, sintering needs to be employed to decompose the organic stabiliser of the ink to then achieve a continuous percolating network.[22,58] The conventional method of sintering metallic nanoparticles is thermal sintering.[20,59] Exposure of printed patterns to elevated temperatures removes organic additives and enhances self-diffusion of surface atoms of nanoparticles, resulting in initial neck formations between adjacent nanoparticles and percolation networks below melting temperature. However, thermal sintering is usually inapplicable to flexible substrates due to high applied temperatures. Selective laser sintering is a promising alternative.[23,39] The particles near the surface absorb the energy of the focused laser beam, generating localized heat by the induced photothermal effect and leading to rapid sintering. Heat transferred from the top sinters the underlying nanoparticles without damaging the substrate. The surface morphology of laser and thermal sintered metallic nanoparticles look very similar.[39]

For liquid metal nanoparticles, although there is no chemical agent, the oxide skin (primarily Ga_2O_3) prevents the particles from spontaneously coalescing. The estimated resistivity of Ga_2O_3 surrounding bulk eGaIn is around 10^6 Ω cm,[60] which is about 10 orders of magnitude less conductive than eGaIn itself (29.4×10^{-6} Ω cm), and electrically insulates the particles from their neighbors. This contact resistance leads to electrical losses and renders the particle film non-conductive. The oxide skin needs to be ruptured in order to allow liquid metal cores flow out and coalesce into conductive pathways. Previous work using liquid metal particles has relied on mechanical sintering methods,[57] which put a lower bound on both the size of the particles and softness of the substrate that may be utilized.[11] The resolution of the mechanically sintered patterns was also limited.[11,61,62]

Recently, we showed that laser sintering of liquid metal nanoparticles results in conductive patterns, and that the laser sintering technique is fast, scalable, and boundless.[63] We hypothesized that the observed coalescing phenomenon can be attributed to ablation (i.e., vaporization) of the metal oxide shell induced by the heated liquid metal core, or to the rupture of the metal oxide shell due to thermal expansion of the liquid metal core relative to the shell. Our previous work also found that the uncoalesced particles underneath the coalesced particles on the top surface of the film were conductive up to an effective sintering depth.[63] However, the reason for this phenomenon was unclear, and the sintering mechanisms, structure and properties of the resulting films were not fully studied yet. Furthermore, Cutinho et al.[55] demonstrated that by simply applying heat to liquid metal microparticles, rupture of the oxide shell and phase segregation occurred due to thermal expansion and surface oxidation. Changes in surface roughness, surface composition and oxidation were also observed.[55] The published work implies that, as two thermally involved methods, laser and thermal sintering both involve rupturing of the gallium oxide shell, but the resulting film morphology and properties may be different.

While laser sintering of liquid metal nanoparticles has been demonstrated in our previous work,[63,64] there has not been any work done to investigate the changes in electrical conductivity of liquid metal nanoparticle films during thermal sintering. Furthermore, the comparison between these two methods in terms of mechanism, resulting film structure and properties has never been studied. A comprehensive examination and evaluation is required to help us further confirm the hypothesis for the laser sintering mechanism, understand the thermal characteristics of liquid metal nanoparticles and exploit these sintering methods to create electronics with desired properties.

In this work, we compare two thermally involved sintering methods by thermal heating liquid metal nanoparticles in an enclosed furnace at varying temperatures, and selectively laser irradiating liquid metal nanoparticles using various laser parameters, all in ambient environment. Both methods result in conductivity of the liquid metal nanoparticle films, but the working mechanisms and resulting film structure and properties are different. Simultaneous differential scanning calorimetry–thermo gravimetricanalysis (DSC–TGA) measurements are performed to examine the thermal characteristics of liquid metal nanoparticle film under different temperatures. The

thermal and laser sintered films are compared with respect to electrical conductivity, surface morphology and elemental composition, crystallinity and surface composition. Moreover, the observation from previous work[63] that uncoalesced particles below the laser sintered trace on the top surface become conductive is explained. Finally, high-resolution laser sintered conductive patterns are demonstrated.

2   Results and discussion

2.1   Preparation and processing

Liquid metal nanoparticle inks were created by sonicating bulk eutectic gallium–indium alloy (eGaIn, 75.5% Ga–24.5% In) in ethanol for 120 min, resulting in particles with average diameters of 220 nm as characterized by Lear *et al.*[65] Subsequently, the nanoparticle inks were deposited onto substrates by spray printing, creating a non-conductive nanoparticle film. For laser sintering, we used a UV laser micromachining system (Protolaser U4, LPKF) with a wavelength of 355 nm, a pulse duration of 900 ns and a beam diameter of 15 μm, operated in ambient environment. Thermal sintering processes were conducted in an enclosed furnace (Thermo Fisher Scientific) in ambient condition. The nanoparticle films were deposited on ceramic substrates, placed in the furnace for 30 min at a certain temperature and then cooled down in air.

2.2   Thermal characteristics under different temperatures

Prior to comparing the two thermally involved sintering processes, we performed simultaneous DSC–TGA measurements in both air and inert atmosphere (argon gas) to examine the thermal characteristics of liquid metal nanoparticles by heating up from 200 °C to 900 °C at a heating rate of 10 °C min^{-1} (Fig. 1). The black curve is the weight gain percentage, and the red curve is the changes in heat flow with temperature.

In air environment, the weight of the nanoparticles stays constant, or shows a very slight increase at temperatures below 300 °C. The evident weight gain of the nanoparticles begin to show at ~340 °C where the prominent increase in both TGA and DSC curves are observed, indicating the beginning of oxidation. The fastest reaction occurs at ~463 °C where the slope of the TGA curve reaches maximum, while the first DSC peak is detected, possibly corresponding to the exothermic oxidation reaction. The weight of the nanoparticles continues to increase rapidly until ~486 °C in the TGA curve where the second DSC peak is detected. The following slope decrease of the TGA curve indicates the decrease of the oxidation rate. We speculate that the second DSC peak corresponds to crystallization of the nanoparticles oxide shells from amorphous Ga_2O_3 to β-Ga_2O_3. The crystallization enhances structural order and packing density of the oxides of the nanoparticles near the surface, making further oxidation of the particles deeper in the film slower. The total weight gain of the nanoparticles after the thermal heating process is ~12.65%.
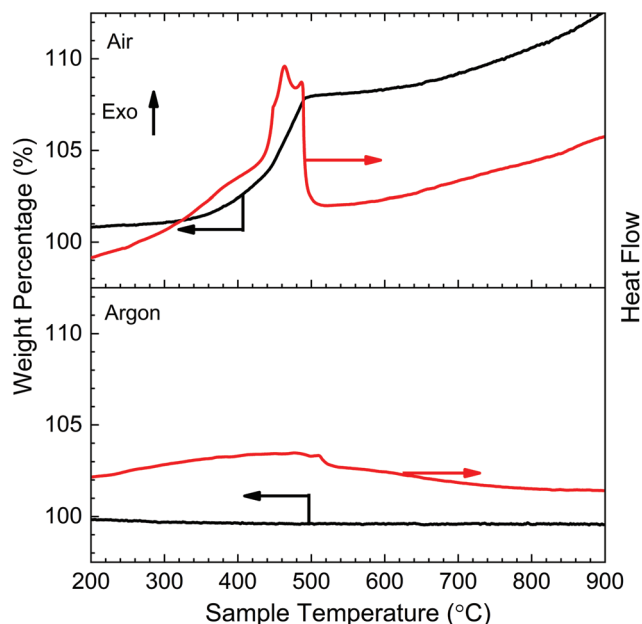

Fig. 1 Simultaneous DSC–TGA measurements of liquid metal nanoparticles heated up to 900 °C from 200 °C at a heating rate of 10 °C min^{-1}. The black curve is the weight gain percentage, and the red curve is the changes in heat flow.

In order to prove our speculation, we further performed TGA and DSC analysis in an argon gas atmosphere by eliminating the oxidation effect. The weight of the nanoparticles stays constant throughout the heating process, which indicates no oxidation. Therefore, the small DSC peak at ~510 °C likely corresponds to crystallization of the Ga_2O_3 shells of the nanoparticles. The crystallization temperature in argon is ~24 °C higher than in air. Variations in the crystallization temperatures in different heating atmosphere have been observed in other materials, which could be due to changes in chemistry, residual stresses, activation energy *etc.*[66,67] Moreover, exothermic energy release (area under the heat flow curve) for this crystallization peak is much lower in argon than in air, likely due to the fact that the Ga_2O_3 layer is much thinner since oxidation is inhibited.

2.3   Electrical properties

We measured resistance values *via* four-terminal resistance sensing on laser and thermal sintered dogbone patterns (7 × 1.4 mm). For the laser process, pre-designed dogbone patterns were directly sintered on liquid metal nanoparticle films deposited on polydimethylsiloxane (PDMS) substrates. We varied laser fluence (optical energy delivered per unit area, 1.52, 1.89, 2.31, 3.11, 4.4, 6.01, 8.49 J cm^{-2}) and beam pulse overlap (the percentage amount of overlap between the diameters of two consecutive pulses, 40, 50, 60, 70, 80, 90%). The beam pulse overlap is a function of the laser beam diameter, scanning speed and pulse frequency. Detailed information and the calculation of the selected laser sintering parameters are included in the ESI.†
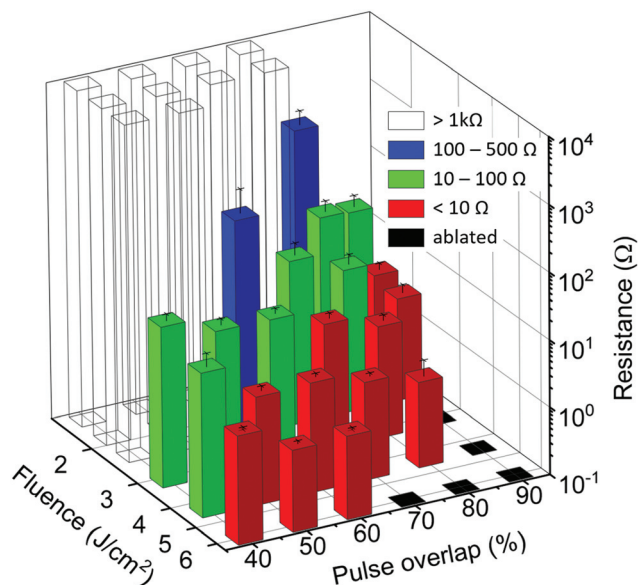
Fig. 2 A 3D bar graph showing the changes of resistance with varying laser fluence and pulse overlap of spray printed liquid metal nanoparticle films. The z-axis is log scale. Different colors represent resistance in different ranges. Error bars represent 95% confidence interval. At high fluence and overlap (black), liquid metal nanoparticles are ablated.
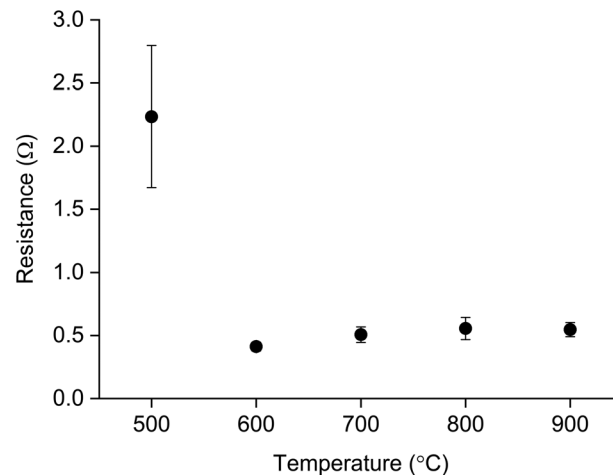

Fig. 3 The changes of resistance with varying heating temperatures of liquid metal nanoparticle films. Error bars represent 95% confidence interval. Particle films heated at 300 °C and 400 °C are not conductive.

Fig. 2 shows the change in measured resistance with varying laser fluence and pulse overlap. As laser fluence or pulse overlap increases, resistance values decrease, since more particles are coalesced as more energy is absorbed by the particles during sintering. At a low laser fluence with low pulse overlap, the employed laser energy is insufficient to sinter liquid metal nanoparticles into conductive patterns, and the measured resistance values are $\sim10^3$ Ω to $\sim10^6$ Ω (transparent bars). Sintered films with resistance values lower than 100 Ω start to appear when pulse overlap is increased to 90% or 80% at a fluence of 1.52 J cm^{-2} or 1.89 J cm^{-2} (green bars). At intermediate laser fluences (3.11 J cm^{-2} and 4.4 J cm^{-2}), low resistance values below 10 Ω are attained when moderate pulse overlap (60%–80%) is applied (red bars). High laser fluence with high pulse overlap causes ablation of liquid metal nanoparticle films (black).

Laser sintered liquid metal nanoparticle films with distinct resistance values can be achieved by tuning laser parameters. Although we have shown this capability using an ytterbium pulsed fiber laser in previous work,[63] the current UV micromachining system certainly has more advantages. With the ability to tune not only laser fluence, but also scanning speed (330–1800 mm s^{-1}) and pulse frequency (160–260 kHz) in a wide range, we are able to attain conductive patterns more rapidly with less energy applied, and an extensive range of resistance values for different potential applications.

For the thermal sintering process, PDMS was used as a mask to pattern dogbone shapes of the same sizes (7 × 1.4 mm) onto a ceramic substrate before spray printing and heating the liquid metal nanoparticle film in the furnace.

Details about the fabrication process are included in the Experimental section. We varied thermal heating temperatures from 300 °C to 900 °C at 100 °C increments. At each temperature, resistance values of ten samples were measured and averaged. Fig. 3 shows the change of resistance with varying heating temperatures. Liquid metal nanoparticle films heated at 300 °C and 400 °C do not show any conductivity. The particle films become conductive after heating at 500 °C, and the resistance value is very low (2.23 ± 0.56 Ω, mean ± 95% confidence interval). At 600 °C, the resistance value drops to 0.41 ± 0.33 Ω and only slightly changes from 700 to 900 °C. The plot indicates that liquid metal nanoparticle films can attain conductivity *via* thermal treatment above 500 °C. From dimensions of the dogbone pattern (length/width = 5) and the sample thickness (~10 μm), resistivity of the thermal sintered films is calculated to be in the range of 8 × 10^{-5}–4.5 × 10^{-4} Ω cm. However, dissimilar to laser sintering, the resistance values are unable to be tuned by varying heating temperature, which implies a different mechanism. To further investigate the cause of conductivity during thermal treatment, liquid metal nanoparticle film structure and composition are studied.

2.4 Effect of laser parameters and heating temperatures on surface morphology and elemental composition

Liquid metal nanoparticle films processed at different laser parameters (fluence and pulse overlap), and heating temperatures are studied. Fig. 4 illustrates the mechanism of laser and thermal sintering liquid metal nanoparticle films. Both methods impart thermal energy to the films and generate thermal stress in the particles, leading to rupture of the gallium oxide shells. However, due to different extents of surface oxidation and oxide rupture, the resulting surface morphologies are different. Typical processes that the particles undergo include thermal expansion, anisotropic contraction, extensive oxide rupture or phase segregation and local oxide
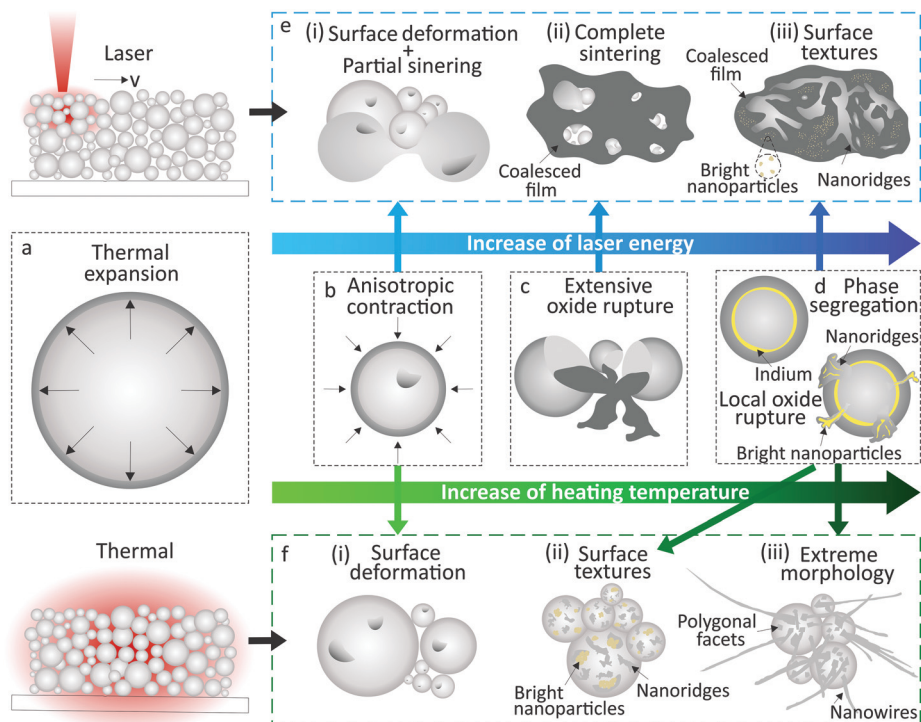
Fig. 4 Schematic demonstrating the mechanism of laser and thermal sintering liquid metal nanoparticle films. Typical processes that the particles experience during laser and thermal sintering are illustrated in a–d. The surface morphologies of laser and thermal sintered films are illustrated in e(i–iii) and f(i–iii), respectively. The direction of the arrows represent the increase of laser energy (blue) and heating temperature (green). At first, both laser and thermal processes induce thermal expansion of the liquid metal core relative to the oxide shell (a). As the oxide grows thicker with increase of energy, anisotropic contraction of the particles occurs during cooling (b). Dimple-like surface deformations are observed on the particles (e(i) and f(i)). Partial sintering of some adjacent particles are observed on the laser sintered film at low laser energy (e(i)). As laser energy increases, laser irradiation causes extensive rupture of the oxide skin of the particles (c), allowing liquid cores to flow out and merge into continuous structures (e(ii)). When laser energy further increases, due to phase segregation and local oxide rupture (d), two types of surface textures are observed on the laser coalesced film (e(iii)): large nanoridges and small, bright nanoparticles. Similar textures are observed on the thermal sintered film as temperature increases (f(ii)). When heating temperature is very high, extreme particle morphology is observed (f(iii)).

rupture, as illustrated in Fig. 4a–d. The surface morphologies of laser sintered films with increasing laser energy and thermal sintered films with increasing heating temperature are illustrated in Fig. 4e(i–iii) and f(i–iii), respectively. Extensive oxide rupture (Fig. 4c) only occurs in the laser sintering process where as oxide ruptures, liquid metal cores flow out and coalesce into conductive pathways. The scanning electron microscopy (SEM) images of laser and thermal sintered liquid metal nanoparticles films are presented in Fig. 5–7. For some selected sintering parameters, energy dispersive X-ray spectroscopy (EDS) elemental mappings are included to identify the spatial distribution of elements.

2.4.1 Effect of low laser energy and heating temperature. Prior to examining conductive structures achieved by laser and thermal sintering, we compare the morphologies of laser and thermal processed liquid metal nanoparticle films at low fluence (1.52 J cm^{-2}, 70%) and temperature (300 °C) where the films are still not conductive. The resistance of the laser sintered film (Fig. 5a) is around ~10^6 Ω, while the thermal heated film (Fig. 5b) is completely non-conductive. As shown in Fig. 4e(i), f(i) and 5, morphologies of the films processed at

these two conditions appear very similar. Most of the particles are still isolated, and no visible continuous pathways are formed to create electrical connections. Moreover, dimple-like surface deformations are observed on the particles. We postulate that as the oxide skin grows thicker during heating, differences in thickness, hence thermal expansion and elasticity of the oxide (Fig. 4a), lead to anisotropic contraction of the particles during the subsequent cooling process (Fig. 4b). Cutinho *et al.* presented a similar phenomenon on liquid metal microparticles heated at 300 °C.[55]

For the laser sintered film (Fig. 4e(i) and 5a), the particles are bigger and the film is more compact. It suggests that despite insufficient laser energy overall to sinter all the particles, the very high peak energy focused on the small areas may generate enough thermal stress in the particles to break the oxide and coalesce some adjacent particles. The reduced contact resistance among the particles contributes to the slightly conductive reading of the laser sintered film. These results indicate that the effects of laser and thermal sintering on the particle films are similar when oxide rupturing and oxidation are not prominent.
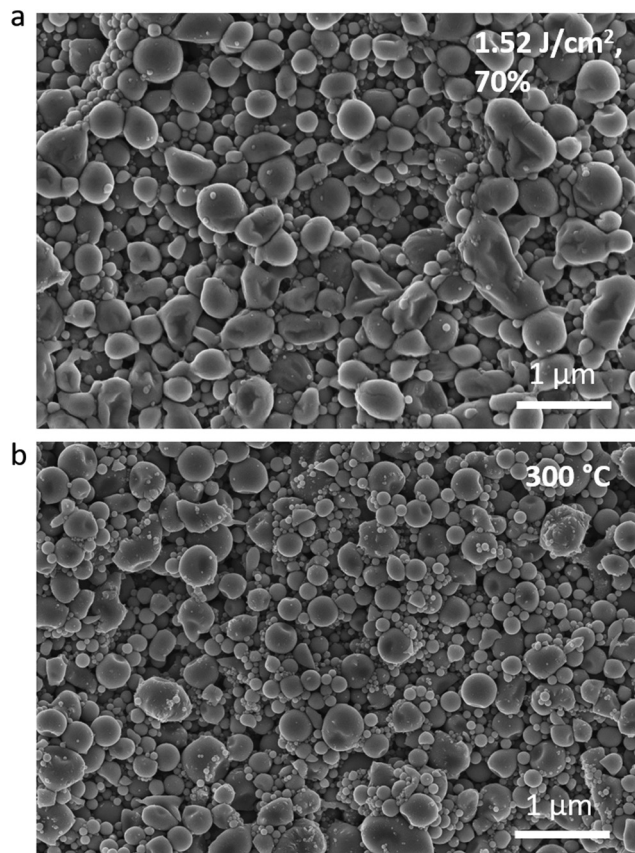
Fig. 5 Surface morphology comparison of non-conductive liquid metal nanoparticle films after laser irradiation and thermal heating at low laser fluence (1.52 J cm^{-2}, 70%) (a) and low heating temperature (300 °C) (b).

2.4.2 Effect of different laser parameters. In contrast to the conventional solid metallic nanoparticles, surface morphologies of laser and thermal sintered liquid metal nanoparticle films diverge at the appearance of electrical conductivity. As shown in Fig. 6, when supplied laser energy increases (in the direction of the arrow), the sintered films start to become more conductive, and surface morphologies change significantly. At 1.89 J cm^{-2} laser fluence and 80% pulse overlap, the resistance of the sintered pattern is 46.35 Ω. Comparing to Fig. 5a where most of the particles are disconnected, the morphology shown in Fig. 6a exhibits a partially sintered structure with much larger coalesced particles in micron scale. When laser fluence is further increased to 3.11 J cm^{-2} with a pulse overlap of 50%, the resistance is reduced to 13.84 Ω. As seen in Fig. 6b, a fully connected liquid metal network is formed, suggesting that stress generated by the photothermal effect of the laser beam is sufficient to cause extensive rupture of the oxide skin of the particles (Fig. 4c), allowing liquid cores to flow out and merge into continuous structures (Fig. 4e(ii)). As laser fluence is further increased to 4.4 J cm^{-2} with 80% overlap, the resistance drops to 1.86 Ω. The SEM image in Fig. 6c indicates that as more laser energy is delivered during sintering, more particles are coalesced

across the film, forming large protruding networks due to high surface tension of liquid metal.

While the sintered structures seen in Fig. 5a and 6a, b are generally smooth, non-uniform surface textures begin to appear at high laser fluence, as illustrated in Fig. 4e(iii). Fig. 6d shows a detailed view of the textures appearing on the surface of the coalesced network in Fig. 6c. Two types of surface textures are observed: large nanoridges with length scales on the order of hundreds of nanometers and small, bright particles with lengths on the order of a few tens of nanometers (inset). The elemental mapping in Fig. 6e shows that gallium and indium are well distributed over the entire selected region, while oxygen is more concentrated in the areas with nanoridges. When laser energy is high, the oxide skin is more permeable to oxygen due to thermal expansion, causing it to become thicker and more brittle. We hypothesize that during cooling, rather than undergoing surface deformations at low laser energy, the oxide skin ruptures locally, allowing liquid metal cores or the underlying gallium layer to flow out. Then, the released metal quickly forms an oxide skin on the surface which stabilizes them in the shape of nanoridges (Fig. 4d). This hypothesis is supported by the elemental mapping as shown in Fig. 6e, which shows a higher oxygen concentration in the regions with nanoridges as induced by growth of the new oxide layer on the nanoridges over the previous oxide layer underneath. The small, bright nanoparticles are too small to be detected by EDS.

It is known that gallium is easier to oxidize than indium.[68,69] In addition, previous X-ray reflectivity studies by Regan et al.[70] concluded that there is a segregated indium layer underneath the surface oxide, consistent with the Gibbs adsorption rule.[71] At some specific regions where more gallium is oxidized on the surface, more indium from the core can be segregated to the surface in order to keep the core at the eutectic composition. Therefore, we speculate that the small, bright nanoparticles (Fig. 6d inset) have more indium content that is released as the oxide ruptures during cooling. Liquid cores of the coalesced structures after laser sintering were confirmed by scratching the sintered films using tweezers. The SEM images in Fig. S1 (ESI†) show that after mechanically breaking the oxide, the coalesced network reflows into a complete liquid trace.

2.4.3 Effect of different heating temperatures. Interestingly, the surface textures observed from the laser sintered samples at high energy appear similar to the two tiers of texture on liquid metal microparticles thermally sintered at 500 °C presented by Cutinho et al.[55] This suggests that these two thermally involved sintering methods are both associated with oxide rupturing due to surface oxidation and thermal expansion. We further performed thermal treatment on liquid metal nanoparticle films at varying temperatures to examine if electrical conductivity is related to particle coalescence as well. Fig. 7 shows the SEM images of thermal sintered liquid metal nanoparticle films from 500 °C to 900 °C at increments of 100 °C. The EDS elemental mapping of the film heated at 500 °C (Fig. 7a) is also included to identify elemental distri-
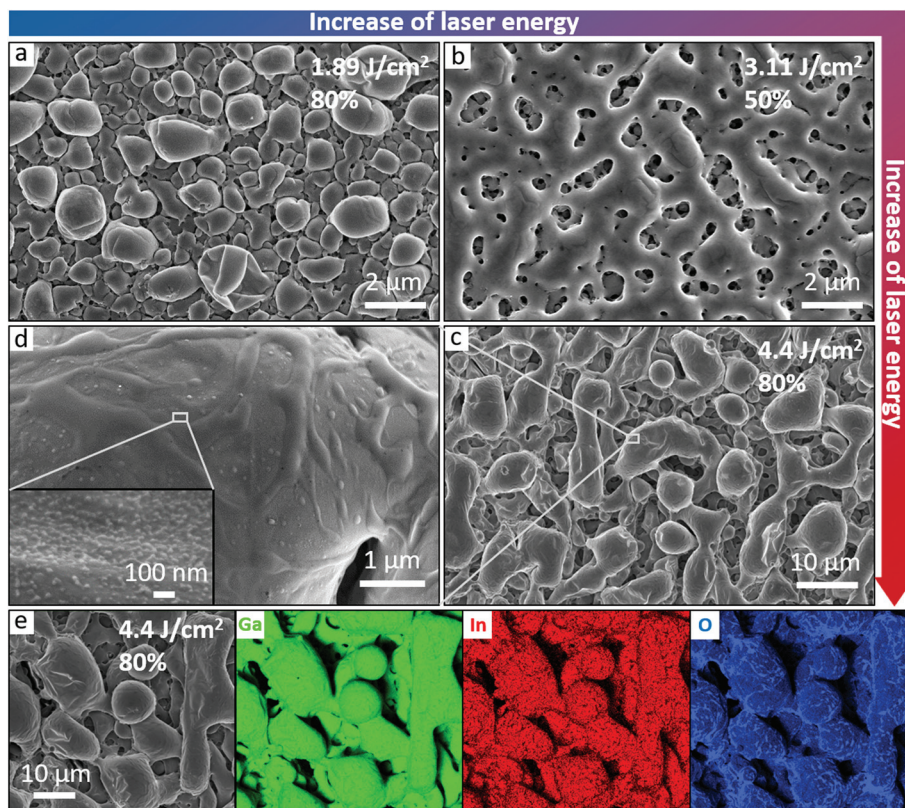
Fig. 6   SEM and EDS analyses of laser sintered liquid metal nanoparticle films, indicating changes in surface morphology and elemental composition at varying fluence and pulse overlap. (a)–(c) SEM images of laser sintered nanoparticle films at 1.89 J cm^{-2}, 80% (46.35 Ω); 3.11 J cm^{-2}, 50% (13.84 Ω); 4.4 J cm^{-2}, 80% (1.86 Ω). The direction of the arrow represents the increase of laser energy. (d) The detailed view of the textures appearing on the surface of the coalesced network in (c). (e) EDS mapping images of liquid metal nanoparticle films sintered at 4.4 J cm^{-2}, 80% (1.86 Ω). Oxygen is more concentrated in the areas with nanoridges.

bution. Furthermore, we scratched the thermal sintered films using tweezers to test the cores of the particles at room temperature. Thermal sintered particles at 500 °C coalesce into a liquid trace which is not fully continuous (Fig. S2, ESI†), indicating a small amount of liquid left in the cores. Above 500 °C, the particle cores are not liquid anymore. Our findings suggest that as we expect, oxidation is much more severe in thermal than laser sintering due to longer exposure to high temperature.

The nanoparticle films thermally sintered at 500 °C appear similar to the microparticles studied by Cutinho et al.[55] The parent particles are covered with rough nanoridges and small, bright nanoparticles with average diameters of 50 nm (Fig. 4f(ii) and 7a). As shown in Fig. S3 (ESI†), the small, bright nanoparticles are well distributed over the entire surface of the film. The sizes of these nanoparticles are ~4–5 times larger than the ones on the laser sintered films shown in Fig. 6d (inset) and can be identified by EDS. The Ga and Ga–In overlay maps in Fig. 7a show that these bright nanoparticles on the parent particles indeed have higher indium content as hypothesized. We speculate that compared to laser sintering, longer exposure to elevated temperatures (30 min) during thermal sintering process induces a higher degree of oxidation, hence a thicker indium segregated layer at the interface, leading to larger and

more extensively distributed indium-enriched particles as the oxide ruptures upon cooling (Fig. 4d). At 600 °C (Fig. 7b), clusters of bright nanoparticles are present at specific regions. The size of a single nanoparticle in the clusters is about the same as 500 °C (~50 nm). The regions with the clusters are more oxidized and have a higher content of indium, as shown in the EDS results in Fig. S4 (ESI†). We hypothesize that due to a higher degree of oxidation, the isolated bright nanoparticles may have formed at first, and then was quickly displaced by Ga_2O_3[72,73] while the adjacent nanoparticles are fused into clusters.

2.4.4   Extreme particle morphology at high heating temperatures. Thermal heating liquid metal nanoparticle films at high temperatures (700 °C–900 °C) induces extreme particle morphology changes, as shown in Fig. 7c–g. We note that similar particle morphology was not observed by Cutinho et al.,[55] and the discrepancy is probably due to different particle sizes (~220 nm vs. 1–5 μm [55]), hence different extent of oxidation and crystallization at high temperature.

At 700 °C (Fig. 7c), bright clusters with bigger nanoparticles (~73 nm) appear on the surface, and nanorods with average diameters of ~25 nm and lengths of 30–150 nm are present. At 800 °C (Fig. 7d), the single nanoparticles in the bright clusters (~153 nm) are about twice as big as the particles that appeared
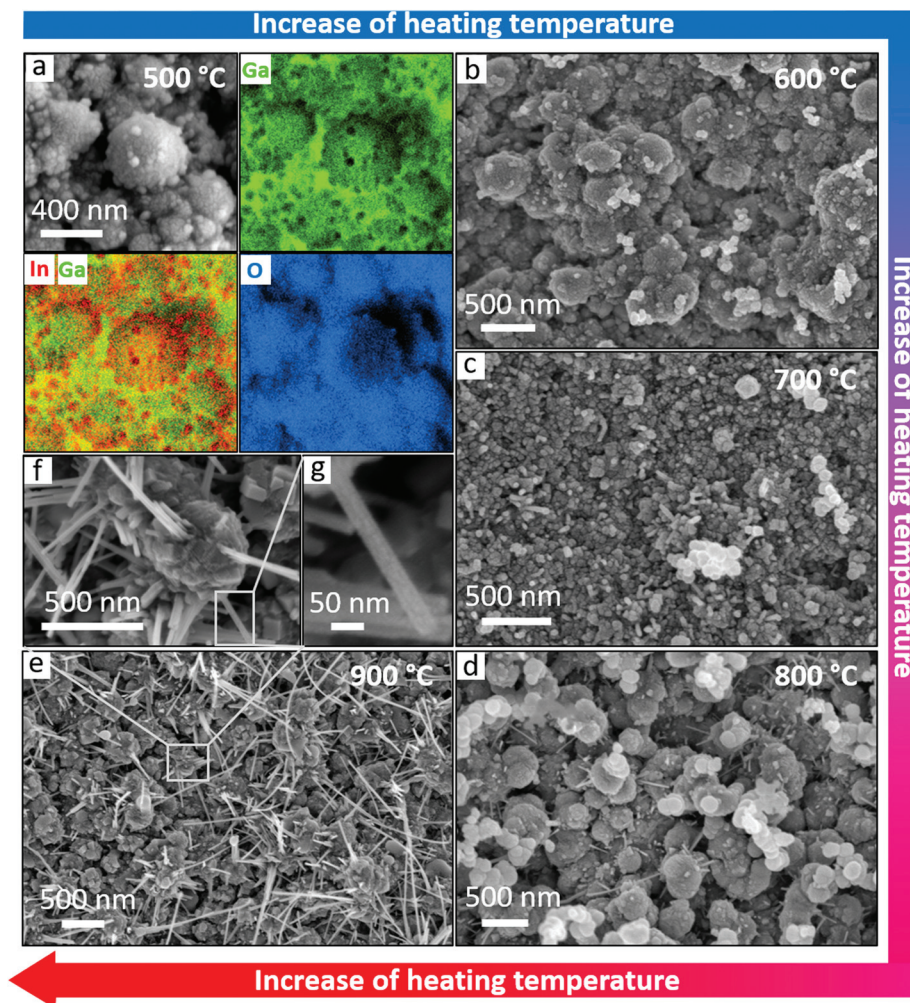
Fig. 7 SEM and EDS analyses of thermal sintered liquid metal nanoparticle films, indicating changes in surface morphology and elemental composition at varying heating temperatures. (a) EDS mapping images of liquid metal nanoparticle films sintered at 500 °C. (b)−(e) SEM images of thermal sintered liquid nanoparticle films at 600 °C, 700 °C, 800 °C and 900 °C. The direction of the arrow represents the increase of heating temperature. (f)−(g) The detailed view of the particles and nanowires shown in (e).

at 700 °C. The EDS spectra in Fig. S5 (ESI†) show that the clusters are highly oxidized. A few polygonal facets and nanowires with average diameters of ∼23 nm and lengths of 50−500 nm are present, as illustrated in Fig. 4f(iii). At 900 °C (Fig. 7e), bright clusters are not observed, whereas a significant amount of polygonal facets are present, implying higher extent of oxidation and crystallization. Bright clusters have likely formed at the early stage and grown into facets or fallen off the surface, as implied in Fig. S6 (ESI†). The observed nanowires have the same average diameters as those appeared at 800 °C, with lengths ranging from 300 nm to 1.7 μm.

In order to study composition of the nanowires, we separated single nanowires from the particles by sonicating a sample thermally sintered at 900 °C in isopropyl alcohol for a few minutes and then drop casted onto a copper grid for imaging. The retention of the nanowires morphology after ultrasonication was confirmed by SEM. The EDS spectra and mappings from the high-angle annular dark-field scanning

transmission electron microscopy (HAADF-STEM) image demonstrate that the nanowries are primarily composed of Ga and O, with a negligible amount of In (Fig. S7, ESI†).

The detailed view in Fig. 7f demonstrates that the nanowires grow out of the facet islands that sprouted from the surface of the particles, resembling urchin-like nanostructures. As shown in the detailed view of the nanowire (Fig. 7g), facets seem to grow on the sides, and no particle is observed on the tip, indicating the inapplicability of the well-known vapor–liquid–solid (VLS) mechanism.[74,75] Previously, researchers have synthesized gallium oxide nanowires with similar structures by heating metallic gallium droplets in air at 750–1000 °C.[76,77] The gallium oxide nanospheres formed on the molten gallium droplets act as nuclei at the early stage of nanowire formation. The underlying gallium provides necessary feeding materials that can react with oxygen in air and take place on these nuclei to form nanowires. The mechanism was described as self-catalytic growth.

To observe the nanowire formation at the early stage and better understand the growth process, liquid metal nanoparticle films were thermally sintered at 800 °C or 900 °C for only 5 minutes. At 800 °C (Fig. S8a, ESI†), only a few nanowires are observed with lengths of 10–300 nm and a few facets are present. The nanowires are grown out of the small, bright nanoparticles on the parent particles. At 900 °C (Fig. S8b, ESI†), both the density and lengths of nanowires on the surface increase (50 nm–1 µm). Bright nanoparticles have likely formed on the parent particles at first, and then oxidized and crystallized into facets where the nanowires are nucleated. The facets on the sides of the nanowires are visually distinct. These findings indicate that at high temperature, the surface of the nanoparticle film is considerably oxidized and crystallized. The facets are acting as a self-catalyst for the growth of nanowires. In the nanowires, oxygen is from air, while gallium is from the parent particles. The nucleation and growth rate of the nanowires are increased with heating temperature and time. In the most extreme case, we thermally sintered the particles at 900 °C for 12 h. As shown in Fig. S9 (ESI†), the density and lengths of nanowires are significantly increased.

It is evident that laser sintered liquid metal nanoparticle films are conductive because as the oxide ruptures, liquid cores of the nanoparticles flow out and coalesce into a continuous liquid network, forming electrical pathways. Unlike laser sintered particles, despite getting more compact, thermal sintered particles are not coalesced and no percolation pathways are observed. Hence, liquid metal nanoparticles cannot be actually "sintered" in a similar way to conventional metallic nanoparticles at elevated temperature due to extensive phase segregation and severe surface oxidation. It is worth noting that particle cores are no longer liquid above 500 °C, which

indicates that the particles are substantially oxidized, hence the low resistance of thermal sintered films may be attributed to gallium or indium oxide. Ramana et al.[78] demonstrated that resistivity of a sputter deposited gallium oxide film significantly drops when it changes from amorphous at room temperature to crystalline structure at high temperature, and resistivity is dependent on crystallinity. Furthermore, researchers presented that resistivity of a deposited indium oxide film also decreases as film crystallinity increases.[79,80] Therefore, to further investigate the source of conductivity, we examined the crystallinity of gallium and indium oxide of laser and thermal sintered liquid metal nanoparticle films.

2.5 Crystalline phases

X-ray diffraction (XRD) analysis was conducted to identify crystalline phases of laser (Fig. 8a) and thermal (Fig. 8b) sintered liquid metal nanoparticle films. Researchers have found that it is significantly easier to form an amorphous gallium oxide on a disordered structure like liquid metal.[70,81] The diffraction pattern at the bottom of Fig. 8b confirms that as-printed liquid metal nanoparticles are completely amorphous. As shown in Fig. 8a, at varying laser parameters, none of the samples show any crystalline peaks, indicating that all the laser sintered nanoparticle films stay amorphous. This data is in accordance with our previous investigation that after laser sintering, the coalesced structures are still at the eutectic composition.

Moreover, since the detection depth of XRD is beyond the top sintered region (~800 nm),[63] the uncoalesced particles (including their oxide layers) underneath are amorphous as well. In previous work, we noticed that the uncoalesced particles underneath the coalesced particles on the top surface of the film were conductive up to an effective sintering depth.[63]
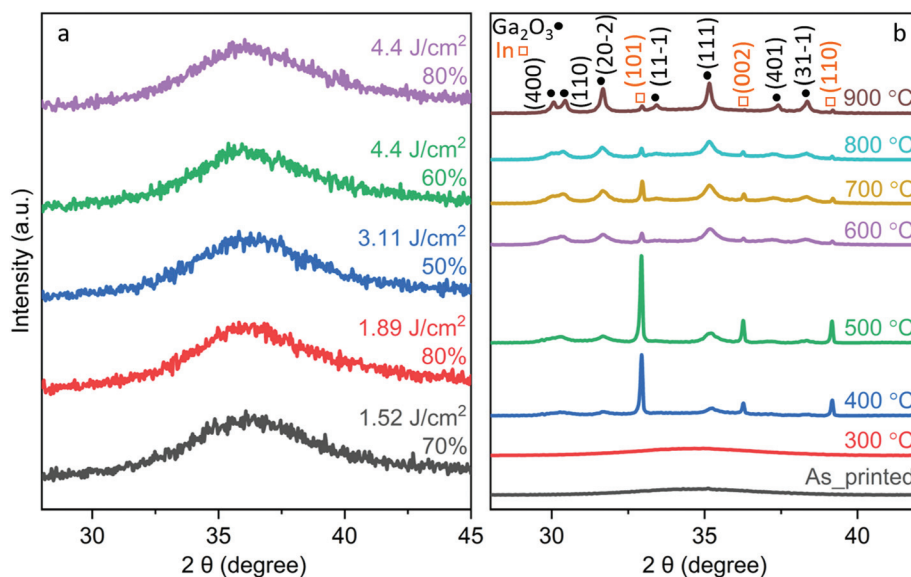

Fig. 8   X-ray diffraction patterns of (a) laser sintered liquid metal nanoparticle films at varying laser fluence and pulse overlap; (b) thermal sintered liquid metal nanoparticle films at varying temperatures and as-printed liquid metal nanoparticle films. The effect of applied laser energy and heating temperature on the evolution of the patterns can be seen.

Hence, the conductivity of the uncoalesced particles is not attributed to the crystallinity change of the surface oxide. The cross-section images in Fig. S10 (ESI†) show that comparing to non-conductive as-printed liquid metal nanoparticles (Fig. S10a and b, ESI†), the uncoalesced particles underneath the top coalesced regions of the laser sintered samples are more closely packed due to partial sintering from the instantaneous heating with the laser beam (Fig. S10c–f, ESI†). The partial sintering phenomenon is more evident on the particle films sintered at high laser energy 4.4 J cm^{-2}, 80% (Fig. S10e and f, ESI†). In this case, contact resistance among the particles is reduced, hence the surface oxide has less effect on the overall conductivity of the film.

For thermal sintering, no crystalline peaks are observed in the films heated up to 300 °C, suggesting no crystallization or phase segregation at this point. Diffraction peaks start to appear when heating to 400 °C, indicating the beginning of oxidation and phase segregation, which is in accordance with the simultaneous DSC–TGA measurements (Fig. 1). The identified peaks (101), (002), (110) at 2θ values of 32.95, 36.27 and 39.18 correspond to tetragonal indium (space group $I4/mmm$, PDF #00-005-0642). At 500 °C, the intensities of these indium peaks increase while the peak widths are reduced. This data confirms our hypothesis that as temperature increases, surface oxidation is accelerated, leading to more indium from the eutectic core segregated to the interface and eventually formed into indium-enriched bright nanoparticles as the oxide ruptures (Fig. 7a). Moreover, peaks located at 30.32, 31.72, 35.22 and 38.34 corresponding to monoclinic β-Ga_2O_3 (space group $C2/m$, PDF #01-087-1901) (400), (20-2), (111) and (31-1) start to get pronounced at 500 °C, which is close to the temperature of the crystallization peak observed in the DSC curve (Fig. 1). The intensities of these peaks gradually increase and become sharper as temperature increases, which indicates high crystalline structure. When maximum heating temperature (900 °C) is reached, these peaks exhibit distinctively high intensities, and additional diffraction peaks of β-Ga_2O_3 (110), (11-1) and (401) located at 30.46, 33.44 and 37.44 are evident. The relative peak intensity is consistent with the reported pattern (PDF #01-087-1901).

Our findings agree with the literature that Ga_2O_3 films deposited at high temperatures (>500 °C) become crystalline, and the crystallinity of Ga_2O_3 is enhanced with temperature due to improved structural quality and packing density.[78,82,83] The amorphous nature of Ga_2O_3 on thermal sintered films below 500 °C and laser sintered films can be attributed to insufficient thermal energy to promote structural order. The demonstrated crystallinity of gallium oxide supports our conjecture that conductivity of the thermal sintered films above 500 °C is in large part attributed to gallium oxide. Segregated indium may contribute to the conductivity as well, whereas indium oxide and gallium peaks are not observed, likely because of poor crystallinity or small quantity. In addition, the XRD pattern of the nanoparticle films sintered at 900 °C for 12 h (Fig. S11, ESI†) shows that while the intensities of (20-2) and (111) are still high, the intensity of (400) increases significantly, which may indicate that the observed nanowires have a preferred growing direction.

2.6 Surface composition analysis

We also performed an X-ray photoelectron spectroscopic (XPS) analysis to characterize the surface composition of liquid metal nanoparticle films after laser and thermal sintering. Since the maximum detection depth of XPS is ~10 nm, all the signals are within single nanoparticles and representing composition at the top surface. The core level XPS spectra of gallium and indium are shown in Fig. 9a, b, d and e (Ga 3d, In 3d) and Fig. S12† (Ga 2p) in the ESI.† In order to quantify surface composition, relative concentration of gallium oxide (Ga_2O_3) vs. elemental gallium (Ga) and total gallium (Ga + Ga_2O_3) vs. total indium (In + In_2O_3) are calculated from scaled peak area ratios and plotted against laser parameters and heating temperature as shown in Fig. 9c and f. With the accessibility to measure both Ga and Ga_2O_3 concomitantly, Ga 3d region was selected to obtain the Ga/Ga_2O_3 ratio in order to investigate the extent of surface oxidation at different conditions. To make a direct comparison, the spectra shown in Fig. 9a and d are normalized to the maximum peak intensity. The total Ga is obtained from Ga 2p spectra (Fig. S12, ESI†) where Ga and Ga_2O_3 are indistinguishable. The total indium is obtained from In 3d spectra (Fig. 9b and e) by adding up both In and In_2O_3 signals.

The relative peak areas (Fig. 9a) and the calculated ratios (Fig. 9c) of Ga/Ga_2O_3 show that as laser energy increases, signals from elemental Ga decrease relative to Ga_2O_3, indicating that gallium on the surface is more oxidized. Furthermore, as shown in Fig. 9b, at the lowest laser energy, indium peaks are positioned at ~450.5 eV (In 3d3) and ~443.9 eV (In 3d5), which correspond to elemental In. However, with increasing laser energy, while elemental In peaks are still visible, the peaks positioned at ~452.9 eV and ~445.6 eV corresponding to In_2O_3 start to appear and dominate at the highest selected laser energy. As seen in the plot of concentrations (Fig. 9c), at first, the amount of total In decreases relative to total Ga (red curve) since more gallium is oxidized on the surface (black curve). However, as applied laser energy further increases, total In concentration increases (red curve). These results further verify our previous speculation that as the surface is more oxidized, more indium is segregated to the interface, eventually forming into indium-enriched bright nanoparticles. These particles quickly oxidize and form thin indium oxide on the surface.

On the other hand, as indicated by the appearance of various surface features at varying temperatures, the surface composition change of thermal sintered liquid metal nanoparticle films is very complicated. Similar to the composition change of laser sintered film at low energy, as the film is heated up to 400 °C, elemental Ga decreases relative to Ga_2O_3 due to more surface oxidation (Fig. 9d and f). In the meantime, elemental In peaks are replaced by In_2O_3 peaks (Fig. 9e), indicating the oxidation of In on the surface. The concentration of total indium signals (In_2O_3 in this case) increases
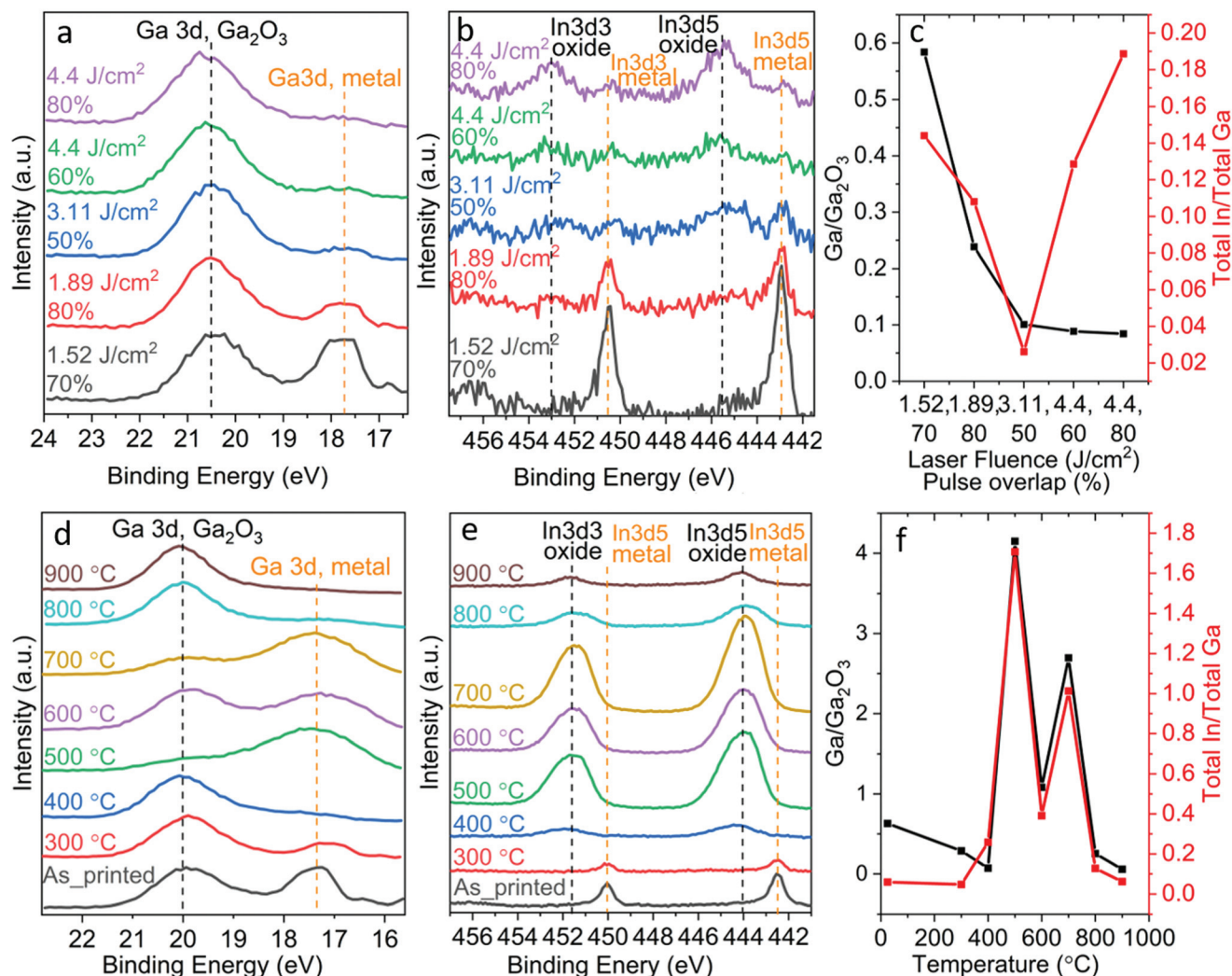
Fig. 9 XPS analysis of laser and thermal sintered liquid metal nanoparticle films. (a) Ga 3d, (b) In 3d core level spectra of liquid metal nanoparticle films sintered at varying laser parameters. (c) The ratio of elemental gallium (Ga)/gallium oxide (Ga_2O_3) and total indium (In + In_2O_3)/gallium (Ga + Ga_2O_3) at varying laser parameters. (d) Ga 3d, (e) In 3d core level spectra of liquid metal nanoparticle films at different heating temperatures. (f) The ratio of elemental gallium(Ga)/gallium oxide (Ga_2O_3) and total indium (In + In_2O_3)/total gallium (Ga + Ga_2O_3) at varying heating temperatures. To make a direct comparison, the spectra shown in (a), (d) are normalized to the maximum peak intensity.

and hits the maximum at 500 °C (Fig. 9f). This data confirms the previous conclusion that indium starts to segregate to the interface at 400 °C and release as small, bright nanoparticles on the surface at 500 °C.

At 600 °C, the ratios of total In/total Ga and Ga/Ga_2O_3 decrease (Fig. 9f). We speculate that due to a higher degree of oxidation, the isolated small, bright nanoparticles are displaced by Ga_2O_3 while the adjacent nanoparticles are fused into clusters and less distributed across the surface. Therefore, surface areas covered with Ga_2O_3 dominate, contributing to more gallium signals. At 700 °C, the concentrations of total In/total Ga, and Ga/Ga_2O_3 increase again (Fig. 9f), which implies that more bright nanoparticles are sintered into clusters and cover the surface. As the surface becomes more crystallized, metallic gallium starts to be driven towards the surface to take place on the nuclei and form nanorods, thus contributing to

more elemental Ga signals relative to Ga_2O_3. As temperature is further increased to 800 °C and 900 °C, almost all the elemental Ga is completely oxidized both in the form of particles and nanowires, so the surface is mostly covered by Ga_2O_3. These results indicate that in thermal sintered films, metallic gallium and indium oxide may also contribute to the conductivity. At high heating temperature (800–900 °C), when the surface is mostly oxidized, conductivity is primarily induced by crystalline Ga_2O_3.

2.7 High-resolution selective laser sintering

This comprehensive comparison confirms that owing to instantaneous irradiation of the laser sintering process, severe oxidation is avoided and large thermal stress is generated. Therefore, oxide rupturing followed by particle coalescence, and resulting conductive patterns in liquid form can be
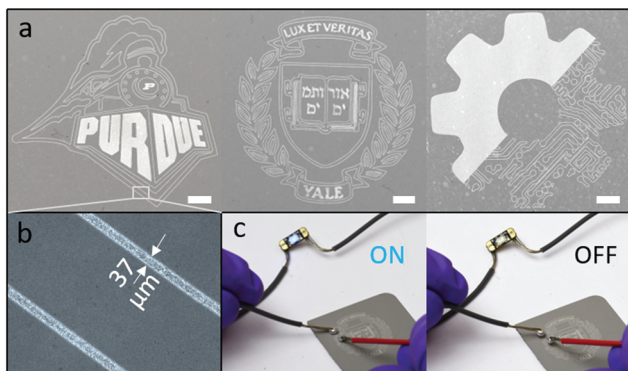
Fig. 10 (a) Demonstration of laser sintered complex conductive patterns: Purdue train, Yale seal and Faboratory gear. Scale bars are 100 μm in length. (b) Optical microscope image showing the minimum width of a single laser sintered trace. (c) Photographs of laser sintered liquid metal patterns acting as circuits to connect LED.

achieved. Previously, we have shown the ability to make flexible, wearable and multilayer circuits using selective laser sintering.[63] However, the minimum width of the traces was ~200 μm, which limits packing density of electronic devices. Here, for the first time we demonstrate the ability to create high-resolution liquid metal patterns by selective laser sintering using a UV laser micromachining system. Fig. 10a shows examples of very intricate patterns in the form of the Purdue University train, Yale University seal and Faboratory lab gear. These patterns can be processed to have both raster-based regions achieved by scanning a pulsed laser spot over an area and vector-based regions achieved by drawing a single trace. The optical microscope image in Fig. 10b shows that the sintered single trace width is as small as 37 μm. As shown in Fig. 10c, these high-resolution traces are conductive and can be employed as electronic circuits to connect LED. Achieving liquid metal patterns with resolution comparable to this is almost unfeasible using other patterning methods including injection into microchannels[73] and masked deposition.[84] Furthermore, the sintering time for each pattern is less than 10 s. The capability of creating precise and high-resolution liquid metal patterns enables miniaturization of soft electronic components that can be implemented to realize small scale and high-density electronics for wearable and soft robotic systems.

3. Conclusions

This work demonstrates two sintering techniques to sinter non-conductive liquid metal nanoparticle films into conductive patterns. The films are sintered either by selective laser sintering or furnace heating in ambient environment. The thermal characteristics of liquid metal nanoparticle films are examined by simultaneous DSC–TGA measurements. Structure and properties of laser and thermal sintered films, including electrical conductivity (4-terminal sensing), surface mor-

phology and elemental composition (SEM/EDS), crystallinity (XRD) and surface composition (XPS) are compared.

These two thermally involved methods both induce rupturing of the gallium oxide shells, and eventually achieve electrical conductivity of the films. When the supplied laser energy or heating temperature is low, the films remain non-conductive, and dimple-like surface deformations are observed on the particles due to anisotropic contraction upon cooling. Nevertheless, the surface morphology diverges as laser energy or heating temperature is further increased. Instantaneous heating with a laser beam generates significant thermal stress in the particles that ruptures oxide skin of the particles extensively, allowing liquid cores to flow out and merge into continuous conductive structures. Despite more oxidation and localized phase segregation at high laser energy, the sintered films stay liquid at all times and the gallium oxide remains amorphous. Conductivity of the uncoalesced particles underneath the top coalesced region is attributed to particle partial sintering and compact packing. On the contrary, in thermal sintering process, particles cannot be coalesced due to much more severe oxidation and less thermal stress. Instead, local oxide rupture and extensive phase segregation occur, resulting in the depletion of liquid cores above 500 °C. Electrical conductivity of the film is caused by crystalline indium and gallium oxide, as well as segregated metal layers. Both sintering methods induce similar surface textures and corresponding surface composition change. Moreover, thermal sintering liquid metal at high temperature induces extreme particle morphology changes.

This comprehensive comparison confirms that oxidation suppression and large thermal stress are indispensable for instantaneous laser irradiating to prevent extensive phase segregation, promote oxide rupturing followed by particle coalescence, and ultimately achieve conductive patterns in liquid form. The laser sintered liquid metal nanoparticle film exhibits superior electrical conductivity and softness. The selective laser sintering process of liquid metal nanoparticles has merits including selective high-resolution patterning (no mask needed), fast sintering speed, and compatibility with soft substrates, which can be employed to create patterns with tunable resistances for soft and flexible electronics with small scale and high density.

For the thermal sintering process, formation of conductive heterogeneous structures including surface textured particles and metal oxide nanowires, have potential applications in the broader semiconductor industry for nanoscale optoelectronic devices, gas sensors or photocatalysis. The thermal sintered liquid metal nanoparticle film presented in this work is not suitable for soft and flexible electronics due to its resulting solid form and strong adhesion to the substrate. However, we found that when the printed film is sufficiently thick, thermal sintering at high temperature forms a very dense oxide layer on the top surface, preventing further oxygen penetration and coalescing the particles underneath. The resulting composite film can be transferred to a soft substrate and applied to the field of soft electronics. Future efforts will focus on combining

laser and laser sintering processes to create high-density integrated soft electronic devices for soft robotics applications.

4. Experimental section

4.1 Preparation of liquid metal dispersion

The liquid metal dispersion was made by depositing 362 ± 5 mg of eutectic gallium–indium alloy (75.5% Ga, 24.5% In, 495425, Sigma Aldrich) into the bottom of a 3 dram glass vial (03-339-10C, Fisher Scientific). 4 mL of ethanol (V1001, Koptec) was then added to the vial by a micropipette (BPP1000, Lagnet BioPette Plus). The top of the vial was covered with Parafilm (52858-076, VWR) to prevent entry of foreign particles into the sample. The tip of the sonicator probe (Q700 with 1/8″ microtip probe, QSonica) was then punched through the Parafilm and positioned approximately 1 mm from the bottom of the glass vial. A water bath held at 6 °C was raised to immerse the vial for keeping the sample cool. The sample was sonicated at an amplitude of 36 μm (30% setting) for 120 min. Just prior to spray printing, each sample was mixed vigorously using a vortex mixer (VortexGenie) for 3 min to ensure uniform dispersion.

4.2 Spray printing of liquid metal dispersion

The nanoparticle ink was then sprayed onto substrate using a customized spray printer. Compressed air was blown over a syringe needle while ink was dispensed at a fixed rate (0.22 mL min^{-1}). The velocity of the printer stage was 7 mm s^{-1}. Details are described in our previous work.[63] Samples for laser and thermal sintering were fabricated by depositing liquid metal nanoparticle inks onto PDMS and patterned ceramic substrates, respectively. PDMS (Polydimethylsiloxane, Dow Corning, Sylgard 184) substrates were fabricated by mixing and then defoaming the elastomer base and the curing agent in a 10 : 1 ratio using a Thinky Mixer (ARE-310, Planetary Centrifugal Mixer) for 30 s each, spin coated onto a glass slide (48382-180, VWR) at 200 rpm for 60 s using a spin coater (G3-8, SCS), and cured in an incubator at 60 °C for 3 h. The patterend ceramic substrates were fabricated by spin coating PDMS at 500 rpm for 60 s, cutting dogbone patterns using an IR laser (Universal Laser Systems VLS 2.30, 30 W, 10.6 μm CO$_2$; vector mode, 50% power, 50% speed) and then peeling off the dogbone shapes before spray printing. Ceramic (nonporous alumina, 8462K25, McMaster-Carr) substrates were cleaned by rinsing with ethanol, isopropanol and distilled water before printing. After spray deposition, the rest of PDMS masks were peeled off before furnace heating.

4.3 Laser sintering

Samples for laser sintering were sintered using a UV laser micromachining system (Protolaser U4, LPKF) with a wavelength of 355 nm, a pulse duration of 900 ns and a beam diameter of 15 μm, operated in ambient environment. The laser fluence was varied between 1.52 to 8.49 J cm^{-2}, and the beam pulse overlap was varied between 40 to 90%. The dogbone and high-resolution patterns were designed in CorelDraw, exported as DXF files and then imported into the software of the laser system.

4.4 Furnace heating

Thermal sintering process was conducted in an enclosed furnace (Thermo Fisher Scientific) in ambient condition. The nanoparticle films were deposited onto patterned ceramic substrates, placed in the furnace for 30 min at a certain temperature and then cooled down in air.

4.5 Material characterization

Simultaneous differential scanning calorimetry–thermal gravimetric analysis (DSC–TGA) measurements were collected on a Setaram Setsys Evolution. The furnace chamber was purged twice (pulling vacuum and backfilling with ultra-high purity Ar) prior to running experiment. The sample chamber was then held at ambient temperature for three additional minutes to avoid thermogravimetric drift during temperature ramp up. The TGA balance was tared immediately prior to the experiment. Eutectic gallium–indium alloy nanoparticles were heated in a 90 μL alumina crucible to 1000 °C at 10 °C min^{-1} in a carrying gas atmosphere of either compressed air or ultra-high purity Ar, flowing at 20 mL min^{-1}. An empty alumina crucible was used as the reference. Mass and heat flow data were collected for each experiment, and the baseline signal was subtracted from an empty sample experiment run immediately prior.

The electrical resistance measurements were made *via* 4-terminal resistance methods using a digital multimeter (5492B, BK Precision). For laser sintered samples, drops of liquid metal were used to interface between the measurement probes and the surface of the sintered pattern to enable good electrical contact without physically disturbing the surface. The values reported in this paper were calculated from triplicate measurements. After resistance measurements, three experimental samples at each processing parameter were selected and used for further characterization.

SEM images were taken by a Hitachi SU8230 UHR Cold Field Emission Scanning Electron Microscope. Surface morphology of these samples were checked under SEM to confirm good condition (no scratch or break) before conducting XRD and XPS characterization. Elemental composition and mappings were obtained by using energy dispersive X-ray spectroscopy (Flat-Quad, Bruker). XRD patterns were collected using a Rigaku Smartlab X-Ray Diffractometer with Cu Kα radiation (8.04 keV, 1.5406 Å). XPS spectra were collected by use of a monochromatic 1486.7 eV Al Kα X-ray source on PHI VersaProbe II X-ray photoelectron spectrometer with 0.47 eV system resolution. The energy scale has been calibrated by use of Cu 2p3/2 (932.67 eV) and Au 4f7/2 (84.00 eV) peaks on a clean copper plate and a clean gold foil. Survey spectra were collected at a constant pass energy of 187.85 eV. The peak positions were corrected with carbon peak C 1s at 284.8 eV. The high-resolution spectra C 1s, O 1s, Ga 3d, Ga 2p, and In 3d were collected at a constant pass energy of 23.5 eV. Samples

for XPS measurements sat in a desiccator under vacuum overnight and then were blown with dry nitrogen before being loaded into the XPS chamber. The data in Fig. 8 and 9 were checked for repeatability and selected as the representative data.

Conflicts of interest

There are no conflicts to declare.

Acknowledgements

References

1 N. Lu and D.-H. Kim, *Soft Robot.*, 2014, **1**, 53–62.

2 R. K. Kramer, *Micro-and Nanotechnology Sensors, Systems, and Applications VII*, 2015, p. 946707.

3 S. Khan, L. Lorenzelli and R. S. Dahiya, *IEEE Sens. J.*, 2015, **15**, 3164–3185.

4 Y. Liu, H. Wang, W. Zhao, M. Zhang, H. Qin and Y. Xie, *Sensors*, 2018, **18**, 645.

5 H. Yang, W. R. Leow and X. Chen, *Small Methods*, 2018, **2**, 1700259.

6 M. Singh, H. M. Haverinen, P. Dhagat and G. E. Jabbour, *Adv. Mater.*, 2010, **22**, 673–685.

7 T. Carey, S. Cacovich, G. Divitini, J. Ren, A. Mansouri, J. M. Kim, C. Wang, C. Ducati, R. Sordan and F. Torrisi, *Nat. Commun.*, 2017, **8**, 1202.

8 N. Raut and K. Al-Shamery, *J. Mater. Chem. C*, 2018, **6**, 1618–1641.

9 Q. Huang and Y. Zhu, *Adv. Mater. Technol.*, 2019, 1800546.

10 L. Li, Y. Bai, L. Li, S. Wang and T. Zhang, *Adv. Mater.*, 2017, **29**, 1702517.

11 M. G. Mohammed and R. Kramer, *Adv. Mater.*, 2017, **29**, 1604965.

12 X. Wang, Q. Lu, C. Chen, M. Han, Q. Wang, H. Li, Z. Niu and J. Chen, *ACS Appl. Mater. Interfaces*, 2017, **9**, 28612–28619.

13 C. Cao, J. B. Andrews and A. D. Franklin, *Adv. Electron. Mater.*, 2017, **3**, 1700057.

14 S. Agarwala, G. L. Goh, T.-S. D. Le, J. An, Z. K. Peh, W. Y. Yeong and Y.-J. Kim, *ACS Sens.*, 2019, **4**, 218–226.

15 A. Marvin, R. Aljoscha, J. A. Qayyum, S. Pestotnik, L. Stepien, A. Abu-Ageel, A. C. U. Brian Wright, J. Albrecht, L. Harle, J. Papapolymerou and T. Schuelke, *IEEE Trans. Compon., Packag., Manuf. Technol.*, 2018, **8**, 1838–1844.

16 D. Angmo, T. T. Larsen-Olsen, M. Jørgensen, R. R. Søndergaard and F. C. Krebs, *Adv. Energy Mater.*, 2013, **3**, 172–175.

17 S. W. Morton, K. P. Herlihy, K. E. Shopsowitz, Z. J. Deng, K. S. Chu, C. J. Bowerman, J. M. DeSimone and P. T. Hammond, *Adv. Mater.*, 2013, **25**, 4707–4713.

18 Z. Li, T. R. Klein, D. H. Kim, M. Yang, J. J. Berry, M. F. van Hest and K. Zhu, *Nat. Rev. Mater.*, 2018, **3**, 18017.

19 Z. Cui, *Printed electronics: materials, technologies and applications*, John Wiley & Sons, 2016.

20 W. Wu, *Nanoscale*, 2017, **9**, 7342–7372.

21 J. Kim, R. Kumar, A. J. Bandodkar and J. Wang, *Adv. Electron. Mater.*, 2017, **3**, 1600260.

22 A. Kamyshny and S. Magdassi, *Chem. Soc. Rev.*, 2019, **48**, 1712–1740.

23 S. Hong, J. Yeo, G. Kim, D. Kim, H. Lee, J. Kwon, H. Lee, P. Lee and S. H. Ko, *ACS Nano*, 2013, **7**, 5024–5031.

24 R. Zhang, M. Engholm, M. Hummelgård, H. Andersson, J. Örtegren and H. Olin, *ACS Appl. Energy Mater.*, 2018, **1**, 7191–7198.

25 E. B. Secor and M. C. Hersam, *J. Phys. Chem. Lett.*, 2015, **6**, 620–626.

26 K. Chen, W. Gao, S. Emaminejad, D. Kiriya, H. Ota, H. Y. Y. Nyein, K. Takei and A. Javey, *Adv. Mater.*, 2016, **28**, 4397–4414.

27 Z. Zhan, R. Lin, V.-T. Tran, J. An, Y. Wei, H. Du, T. Tran and W. Lu, *ACS Appl. Mater. Interfaces*, 2017, **9**, 37921–37928.

28 W. Li, F. Li, H. Li, M. Su, M. Gao, Y. Li, D. Su, X. Zhang and Y. Song, *ACS Appl. Mater. Interfaces*, 2016, **8**, 12369–12376.

29 S. J. Kim, K. Choi, B. Lee, Y. Kim and B. H. Hong, *Annu. Rev. Mater. Res.*, 2015, **45**, 63–84.

30 L. Pan, A. Chortos, G. Yu, Y. Wang, S. Isaacson, R. Allen, Y. Shi, R. Dauskardt and Z. Bao, *Nat. Commun.*, 2014, **5**, 3002.

31 J. Rivnay, S. Inal, B. A. Collins, M. Sessolo, E. Stavrinidou, X. Strakosas, C. Tassone, D. M. Delongchamp and G. G. Malliaras, *Nat. Commun.*, 2016, **7**, 11287.

32 A. R. Abdel Fattah, T. Majdi, A. M. Abdalla, S. Ghosh and I. K. Puri, *ACS Appl. Mater. Interfaces*, 2016, **8**, 1589–1593.

33 M. Park, J. Im, M. Shin, Y. Min, J. Park, H. Cho, S. Park, M.-B. Shim, S. Jeon, D.-Y. Chung, J. Bae, J. Park, U. Jeong and K. Kim, *Nat. Nanotechnol.*, 2012, **7**, 803–809.

34 H. Lehmann, S. Willing, S. Möller, M. Volkmann and C. Klinke, *Nanoscale*, 2016, **8**, 14384–14392.

35 A. J. Kell, C. Paquet, O. Mozenson, I. Djavani-Tabrizi, B. Deore, X. Liu, G. P. Lopinski, R. James, K. Hettak, J. Shaker, A. Momciu, J. Ferrigno, O. Ferrand, J. X. Hu, S. Lafrenière and P. R. L. Malenfant, *ACS Appl. Mater. Interfaces*, 2017, **9**, 17226–17237.

36 Y. Kashiwagi, A. Koizumi, Y. Takemura, S. Furuta, M. Yamamoto, M. Saitoh, M. Takahashi, T. Ohno, Y. Fujiwara, K. Murahashi, K. Ohtsuka and M. Nakamoto, *Appl. Phys. Lett.*, 2014, **105**, 223509.

37 J. H. Park, Y. T. Lim, O. O. Park, J. K. Kim, J.-W. Yu and Y. C. Kim, *Chem. Mater.*, 2004, **16**, 688–692.

38 R. V. K. Rao, K. V. Abhinav, P. S. Karthik and S. Prakash Singh, *RSC Adv.*, 2015, **5**, 77760–77790.

39 J. Kwon, H. Cho, H. Eom, H. Lee, Y. D. Suh, H. Moon, J. Shin, S. Hong and S. H. Ko, *ACS Appl. Mater. Interfaces*, 2016, **8**, 11575–11582.

40 J. Kwon, H. Cho, Y. D. Suh, J. Lee, H. Lee, J. Jung, D. Kim, D. Lee, S. Hong and S. H. Ko, *Adv. Mater. Technol.*, 2017, **2**, 1600222.

41 T. Campbell, R. K. Kalia, A. Nakano, P. Vashishta, S. Ogata and S. Rodgers, *Phys. Rev. Lett.*, 1999, **82**, 4866–4869.

42 T. J. Foley, C. E. Johnson and K. T. Higa, *Chem. Mater.*, 2005, **17**, 4086–4091.

43 U. Männl, C. Van Den Berg, B. Magunje, M. Härting, D. Britton, S. Jones, M. Van Staden and M. Scriba, *Nanotechnology*, 2014, **25**, 094004.

44 S.-H. Park and H.-S. Kim, *Thin Solid Films*, 2014, **550**, 575–581.

45 P. Pulkkinen, J. Shan, K. Leppänen, A. Känsäkoski, A. Laiho, M. Järn and H. Tenhu, *ACS Appl. Mater. Interfaces*, 2009, **1**, 519–525.

46 C. Lee, N. R. Kim, J. Koo, Y. J. Lee and H. M. Lee, *Nanotechnology*, 2015, **26**, 455601.

47 S. Kapoor, *Langmuir*, 1998, **14**, 1021–1025.

48 K. E. Spells, *Proc. Phys. Soc.*, 1936, **48**, 299.

49 F. Geiger, C. A. Busse and R. I. Loehrke, *Int. J. Thermophys.*, 1987, **8**, 425–436.

50 M. Dumke, T. Tombrello, R. Weller, R. Housley and E. Cirlin, *Surf. Sci.*, 1983, **124**, 407–422.

51 F. Scharmann, G. Cherkashinin, V. Breternitz, C. Knedlik, G. Hartung, T. Weber and J. A. Schaefer, *Surf. Interface Anal.*, 2004, **36**, 981–985.

52 Z. J. Farrell and C. Tabor, *Langmuir*, 2017, **34**, 234–240.

53 R. N. Sodhi, P. Brodersen, L. Cademartiri, M. M. Thuo and C. A. Nijhuis, *Surf. Interface Anal.*, 2017, **49**, 1309–1315.

54 L. Cademartiri, M. M. Thuo, C. A. Nijhuis, W. F. Reus, S. Tricard, J. R. Barber, R. N. Sodhi, P. Brodersen, C. Kim, R. C. Chiechi, *et al.*, *J. Phys. Chem. C*, 2012, **116**, 10848–10860.

55 J. Cutinho, B. S. Chang, S. Oyola-Reynoso, J. Chen, S. S. Akhter, I. D. Tevis, N. J. Bello, A. Martin, M. C. Foster and M. M. Thuo, *ACS Nano*, 2018, **12**, 4744–4753.

56 J. N. Hohman, M. Kim, G. A. Wadsworth, H. R. Bednar, J. Jiang, M. A. LeThai and P. S. Weiss, *Nano Lett.*, 2011, **11**, 5104–5110.

57 J. W. Boley, E. L. White and R. K. Kramer, *Adv. Mater.*, 2015, **27**, 2355–2360.

58 S. Wünscher, R. Abbel, J. Perelaer and U. S. Schubert, *J. Mater. Chem. C*, 2014, **2**, 10232–10261.

59 S. Jeong, H. C. Song, W. W. Lee, S. S. Lee, Y. Choi, W. Son, E. D. Kim, C. H. Paik, S. H. Oh and B.-H. Ryu, *Langmuir*, 2011, **27**, 3144–3149.

60 C. A. Nijhuis, W. F. Reus and G. M. Whitesides, *J. Am. Chem. Soc.*, 2010, **132**, 18386–18401.

61 Y. Lin, C. Cooper, M. Wang, J. J. Adams, J. Genzer and M. D. Dickey, *Small*, 2015, **11**, 6397–6403.

62 E. J. Markvicka, M. D. Bartlett, X. Huang and C. Majidi, *Nat. Mater.*, 2018, **17**, 618.

63 S. Liu, M. Yuen, E. L. White, J. W. Boley, B. Deng, G. J. Cheng and R. Kramer-Bottiglio, *ACS Appl. Mater. Interfaces*, 2018, **10**, 28232–28241.

64 S. Liu, M. C.-S. Yuen and R. Kramer, *Flexible Printed Electron.*, 2018, **4**, 015004.

65 T. R. Lear, S.-H. Hyun, J. W. Boley, E. L. White, D. H. Thompson and R. K. Kramer, *Extreme Mech. Lett.*, 2017, **13**, 126–134.

66 A. Karamanov, L. M. Schabbach, E. Karamanova, F. Andreola, L. Barbieri, B. Ranguelov, G. Avdeev and I. Lancellotti, *J. Non-Cryst. Solids*, 2014, **389**, 50–59.

67 S. Sabharwal, *et al.*, *J. Cryst. Growth*, 2001, **222**, 427–430.

68 D. Chatterji and R. Vest, *J. Am. Ceram. Soc.*, 1972, **55**, 575–578.

69 K. Klinedinst and D. Stevenson, *J. Chem. Thermodyn.*, 1972, **4**, 565–573.

70 M. Regan, P. S. Pershan, O. Magnussen, B. Ocko, M. Deutsch and L. Berman, *Phys. Rev. B: Condens. Matter Mater. Phys.*, 1997, **55**, 15874.

71 J. W. Gibbs, *The scientific papers of J. Willard Gibbs, Longmans*, Green and Company, 1906, vol. 1, p. 219.

72 R. C. Chiechi, E. A. Weiss, M. D. Dickey and G. M. Whitesides, *Angew. Chem., Int. Ed.*, 2008, **47**, 142–144.

73 M. D. Dickey, R. C. Chiechi, R. J. Larsen, E. A. Weiss, D. A. Weitz and G. M. Whitesides, *Adv. Funct. Mater.*, 2008, **18**, 1097–1104.

74 Y. Wu and P. Yang, *J. Am. Chem. Soc.*, 2001, **123**, 3165–3166.

75 M. Johnson, S. Aloni, D. McCready and E. Bourret-Courchesne, *Cryst. Growth Des.*, 2006, **6**, 1936–1941.

76 R. P. de Melo Jr., N. T. C. Oliveira, C. T. Dominguez, A. S. Gomes, E. H. Falcão, S. Alves Jr., L. L. da Luz, R. Chassagnon, C. B. de Araújo and M. Sacilotti, *J. Appl. Phys.*, 2016, **119**, 163107.

77 R. Liu, H. Yang, R. Zhang, H. Dong, X. Chen, L. Li, L. Zhang, J. Ma and H. Zheng, *Sci. China, Ser. E: Technol. Sci.*, 2009, **52**, 1712–1721.

78 C. Ramana, E. Rubio, C. Barraza, A. Miranda Gallardo, S. McPeak, S. Kotru and J. Grant, *J. Appl. Phys.*, 2014, **115**, 043508.

79 S. Noguchi and H. Sakata, *J. Phys. D: Appl. Phys.*, 1980, **13**, 1129.

80 W. J. Maeng, D.-w. Choi, K.-B. Chung, W. Koh, G.-Y. Kim, S.-Y. Choi and J.-S. Park, *ACS Appl. Mater. Interfaces*, 2014, **6**, 17481–17488.

81 G. Bo, L. Ren, X. Xu, Y. Du and S. Dou, *Adv. Phys.: X*, 2018, **3**, 1446359.

82 S. S. Kumar, E. Rubio, M. Noor-A-Alam, G. Martinez, S. Manandhar, V. Shutthanandan, S. Thevuthasan and C. Ramana, *J. Phys. Chem. C*, 2013, **117**, 4194–4200.

83 A. K. Battu and C. V. Ramana, *Adv. Eng. Mater.*, 2018, **20**, 1701033.

84 R. K. Kramer, C. Majidi and R. J. Wood, *Adv. Funct. Mater.*, 2013, **23**, 5292–5296.